Nanoscale

PAPER

View Article Online
View Journal | View Issue

Cite this: *Nanoscale*, 2023, **15**, 13603

Building in biologically appropriate multifunctionality in aqueous copper indium selenide-based quantum dots†

Xiling Yang,[a] Yun Li,[a] Peisen Zhang,*[b,c] Lingfei Guo,[a] Xiaoqi Li,[a] Yiyang Shu,[a] Kuiyu Jiang,[a] Yi Hou,[c] Lihong Jing*[b] and Mingxia Jiao*[a]

Advanced nanoplatforms equipped with different functional moieties for theranostics hold appealing promise for reshaping precision medicine. The reliable construction of an individual nanomaterial with intrinsic near-infrared (NIR) photofunction and magnetic domains is much desired but largely unexplored in a direct aqueous synthesis system. Herein, we develop an aqueous phase synthetic strategy for Mn^{2+} doping of ZnS shell grown on Zn–Cu–In–Se core quantum dots (ZCISe@ZnS:Mn QDs), providing the optimal NIR fluorescence quantum efficiency of up to 18.9% and meanwhile efficiently introducing paramagnetic domains. The relaxometric properties of the water-soluble Mn-doped QDs make them desirable for both the longitudinal and transverse (T_1 and T_2) magnetic resonance (MR) contrast enhancement due to the shell lattice-doped Mn^{2+} ions with slow tumbling rates and favoured spin-proton dipolar interactions with surrounding water molecules. Surprisingly, the incorporation of Mn^{2+} ions into the shell is found to significantly enhance the production of reactive oxygen species (ROS) by combining both the chemodynamic and photodynamic processes upon NIR light irradiation, showing great potential for efficient photo-assisted ablation of cancer cells. Furthermore, a broad-spectrum excitation range beneficial for bright NIR fluorescence imaging of breast cancer has been proven and offers high flexibility in the choice of incident light sources. Multiparametric MR imaging of the brain has also been successfully demonstrated *in vivo*.

Received 23rd May 2023,
Accepted 13th July 2023

DOI: 10.1039/d3nr02385k

rsc.li/nanoscale

Introduction

Precision medicine demands advanced theranostic platforms that can provide accurate diagnosis and specific therapy as well as subsequent real-time monitoring of therapeutic efficacy.[1–6] The concept of integration of different functional components into one nanoplatform is widely adopted, which often suffers from unpredictable dissociation of the components in complex biological environments, leading to inaccurate results. Therefore, it is necessary to develop all-in-one materials with built-in functions to fulfill diverse theranostic applications.

Ternary I–III–VI semiconductor nanocrystals or quantum dots (QDs), such as copper indium selenide QDs, have become attractive alternatives to the more well-established Cd-, Pb-, or Hg-containing QDs for *in vivo* applications.[7–12] Apart from their good biocompatibility due to the absence of highly toxic elements, their relatively narrow bulk band gaps allow the tuning of photoluminescence from the visible region all the way up to the near-infrared (NIR) spectral region,[13–19] where penetration through biological tissue is favorable.[20–24] In contrast to binary Cd-free QDs, ternary QDs show composition-dependent optical properties while maintaining similar particle sizes, which endows the QDs with analogous pharmacokinetic behaviors *in vivo*. As a consequence, ternary QDs with NIR emission have been intensively exploited for imaging *in vivo*.[7,9,25,26] Unfortunately, the majority of I–III–VI QDs suffer from far lower photoluminescence quantum yields (PLQYs) compared with their binary counterparts,[27,28] which goes against high sensitivity in terms of imaging. The low PLQY is largely due to the existence of abundant intrinsic defects in ternary QDs, including vacancies, antisite and inter-

[a]*Key Laboratory of Optic-Electric Sensing and Analytical Chemistry for Life Science, MOE, College of Chemistry and Molecular Engineering, Qingdao University of Science and Technology, Zhengzhou Road 53, Qingdao 266042, China. E-mail: jiaomingxia@qust.edu.cn*

[b]*Key Laboratory of Colloid, Interface and Chemical Thermodynamics, Institute of Chemistry, Chinese Academy of Sciences, Bei Yi Jie 2, Zhong Guan Cun, Beijing 100190, China. E-mail: zhangps@iccas.ac.cn, jinglh@iccas.ac.cn*

[c]*College of Life Science and Technology, Beijing University of Chemical Technology, Beijing, 10029, China*

† Electronic supplementary information (ESI) available. See DOI: https://doi.org/10.1039/d3nr02385k

stitial defects related to non-radiative relaxation of photo-excited charge carriers.[29,30] To solve the above problem, Zn alloying has been employed to improve the PLQY of I–III–VI QDs by reducing Cu^+-related defects and restraining the non-radiative recombination.[31] On the opposite side, the generated radicals or heat involved in nonradiative recombination pathways give us the opportunity to use them for photodynamic or photothermal therapy (PDT/PTT).[32,33] For example, in a recent report Li *et al.* demonstrated the successful utilization of $CuInSe_2$-based QDs for simultaneous PDT and PTT of breast cancer tumors.[25]

To endow optical imaging agents with complemental modality such as magnetic resonance imaging (MRI) to overcome their inherent limitation of spatial resolution,[34,35] magnetic components are often chosen to be loaded into QDs by incorporating, chelating or heteroepitaxial growth.[36–41] In these cases, the fluorescence of the QD core is easily deteriorated by the quenching effect of magnetic domains. In contrast, doping magnetic ions into a compatible semiconductor shell of host QDs can further reduce the negative impact of magnetic doping on the QD core, which is a promising way to produce reliable materials with intrinsic fluorescence and magnetism to address the challenge mentioned above.[25,42] For example, Chetty *et al.* reported Mn^{2+}/Gd^{3+} co-doped $CuInS_2$–ZnS QDs for early diagnosis of subcutaneous melanoma through fluorescence, MR, and CT imaging.[42] Apart from acting as an imaging modality, Mn^{2+} ions have been found to play an important role in treatment applications. For example, the Jiang group reported the importance of manganese in antitumor immune responses *via* cGAS–STING to improve the efficacy of immunotherapy.[43] In another report, single-atom Mn on the surface of Ag_2Te QDs was found by Huang *et al.* to exhibit catalytic activity for scavenging reactive oxygen species to alleviate neuroinflammation in the brain.[23] The above research studies indicate that Mn^{2+} ions doped into multinary QDs may have undiscovered influences on the nonradiative recombination processes, which deserves further investigation to better reveal the functions of manganese doping.

Following our previous studies on the synthesis and bioapplication of ternary QDs,[31,44–46] we herein report a green and mild method for preparing NIR-emitting manganese-doped Zn–Cu–In–Se-based QDs under aqueous conditions. Paramagnetic Mn^{2+} ions were chosen to be doped into a ZnS shell epitaxially grown on Zn–Cu–In–Se core QDs to further retain the high NIR PLQY. Mn^{2+} doping effects on both the optical and magnetic properties as well as the structure of QDs were systemically studied. Interestingly, the incorporation of Mn^{2+} ions into the shell of QDs was found to promote the photodynamic processes with the aid of light irradiation, to yield more reactive oxygen species for killing tumor cells. Furthermore, the biocompatible QDs with broad excitation and bright NIR fluorescence were successfully applied for multichannel imaging of breast cancer *in vivo*. Moreover, multiparametric MR imaging of the brain has also been successfully demonstrated *in vivo*.

Experimental

Chemicals

Indium(III) chloride tetrahydrate ($InCl_3{\cdot}4H_2O$, 97%) was purchased from Adamas-Beta. Copper(II) chloride dihydrate ($CuCl_2{\cdot}2H_2O$, ≥99.0%), manganese(II) chloride tetrahydrate ($MnCl_2{\cdot}4H_2O$, 99%), sodium citrate dihydrate (≥99.0%), and L-glutathione (GSH, ≥98.0%) were purchased from Sigma-Aldrich. Selenium (Se, ≥99.999%) and zinc chloride ($ZnCl_2$, 99.999%) were purchased from Aladdin. Anhydrous ethanol, toluene, sodium borohydride ($NaBH_4$, 98%) and NaOH were purchased from Sinopharm Chemical Reagent Co. Ltd. Cell Counting Kit-8 (CCK-8) assay, 3′,6′-di(*O*-acetyl)-4′,5′-bis[*N*,*N*-bis-(carboxymethyl) aminomethyl]fluorescein, tetraacetoxymethyl ester (Calcein-AM), propidium iodide (PI), dimethyl sulfoxide (DMSO), Dulbecco's modified Eagle's medium (DMEM), and fetal bovine serum (FBS) were purchased from Sangon Biotech Co., Ltd, Shanghai, China. Trypsin was purchased from Biosharp, Hefei, China. 2′,7′-Dichlorofluorescin diacetate (DCFH-DA, 97%) was purchased from Bide Pharmatech Co., Ltd. All chemicals and reagents were used as received without any further purification. Milli-Q water (resistivity of 18.2 MΩ cm) was utilized in all experiments.

Synthesis of Zn–Cu–In–Se@ZnS (ZCISe@ZnS) QDs

At the initial stage of the reaction, deionized water was added to a 50 mL three-necked flask and nitrogen was introduced into water to remove oxygen. At the same time, selenium precursor solution was prepared by dissolving selenium powder (1.00 mmol) and $NaBH_4$ (2.35 mmol) in 5.0 mL oxygen-free deionized water for 30 min to obtain a transparent NaHSe solution. For preparing ZCISe QDs with a Zn : Cu feed molar ratio of 1 : 7, $CuCl_2{\cdot}2H_2O$ (0.0109 mmol), $ZnCl_2$ (0.0016 mmol), sodium citrate dihydrate (0.150 mmol), $InCl_3{\cdot}4H_2O$ (0.0375 mmol) and GSH (0.125 mmol) were firstly added to 20.0 mL oxygen-free deionized water. The transparent solution turned burgundy after adding further 300 μL NaHSe solution. Then the reaction was performed at a boiling state for 2 h to obtain ZCISe QDs. For preparing ZCISe@ZnS QDs, Zn precursor solution was prepared by dissolving $ZnCl_2$ (0.0500 mmol) and GSH (0.0500 mmol) in 2.0 mL ultra-pure water, which was then adjusted to a pH value of 4.5 with 1 M NaOH solution. After the unpurified reaction solution containing ZCISe QDs was cooled down to 80 °C, the Zn precursor solution was added to the reaction system, and the pH value of the whole reaction system was adjusted to 6.5. After two hours of reaction at 80 °C, ZCISe@ZnS QDs were obtained. To purify ZCISe@ZnS QDs, the cooled solution mixture was precipitated using 5-folds of ethanol, which was then centrifuged at 8000 rpm for 10 min. The washing process was repeated three times, and finally, the product was re-dispersed in ultra-pure water and stored at 4 °C for subsequent experiments.

Synthesis of Mn-doped Zn–Cu–In–Se@ZnS (ZCISe@ZnS:Mn) QDs

For preparing ZCISe@ZnS:Mn QDs, $MnCl_2$ was used as a Mn precursor and additionally added to Zn precursor solution in

the shell coating process as that for synthesizing ZCISe@ZnS QDs. All other reaction conditions were the same except for a prolonged reaction time of 5 h. For achieving different Mn^{2+} doping ratios, the feed amount of the Mn precursor was changed accordingly: 0.0130 mmol for a Mn feed doping ratio of 12%, 0.0265 mmol for 21%, and 0.0643 mmol for 39%. Here the Mn^{2+} doping ratio was calculated as follows: Mn content divided by the total amount of all cations (*i.e.*, Cu + In + Zn + Mn) of the doped ZCISe@ZnS QDs. The purification process was basically consistent with that for ZCISe@ZnS QDs mentioned above, except that three cycles of ultrafiltration processes (8000 rpm for 10 min) using MPA aqueous solution (0.48 mM) in an ultrafiltration tube of 30 kDa were performed after the washing process with ethanol, in order to completely remove extra free Mn^{2+} ions.

Characterization

Steady-state ultraviolet-visible (UV-Vis) absorption spectra were recorded on a Shimadzu UV-2600 UV-Vis spectrophotometer. Steady-state PL (with an NIRPMT R5509 detector) and time-resolved PL spectra (with a picosecond pulsed diode laser EPL-510) and the absolute PLQYs of the QDs were measured using an FLS1000 fluorescence spectrometer (Edinburgh Instruments, UK). The excitation wavelength for all steady-state measurements was 530 nm. For monitoring the fluorescence stability of the QDs with different Mn^{2+} doping ratios, the samples were stored at 4 °C, and their PL was measured using FLS1000 at a specific time after being warmed to room temperature. The morphologies of the QDs were examined on a JEM-2100F transmission electron microscope (TEM) and high-resolution TEM (HRTEM) at an acceleration of 200 kV. The particle size was determined by averaging at least 300 particles per sample using ImageJ. Powder X-ray diffraction (PXRD) patterns of the samples were recorded on a Rigaku D/Max-2500 diffractometer under Cu Kα1 radiation (λ = 1.54056 Å). X-ray photoelectron spectroscopy (XPS) measurements were carried out on a Thermo-VG Scientific ESCALAB 250Xi spectrometer with a monochromatic Al Kα X-ray source. Electron spin resonance (EPR) spectra were collected at room temperature on a Bruker EMX PLUS spectrometer. The chemical composition of the purified QDs was determined using an inductively coupled plasma optical emission spectrometer (ICP-OES) using Thermo Fisher IRIS Intrepid II XSP.

Relaxivity measurements

Relaxivity measurements were conducted on a 7.0 T Bruker Biospec animal MRI scanner. In detail, a series of aqueous solutions of the QDs with different Cu concentrations were added in small tubes and subjected to an MRI scanner. Different MRI sequences were obtained to evaluate the MRI performance of the QDs. The parameters of T_1-weighted imaging were set as follows: repetition time (TR) = 300 ms, echo time (TE) = 5.01 ms, field of view (FoV) = 35 × 35 mm, and matrix (MTX) = 200 × 200; the parameters of the T_1 map were set as follows: TE = 5.90 ms, TR = 3000, 1500, 1000, 500, 298 ms, and FoV = 35 mm × 35 mm; the parameters of T_2-weighted imaging were set as follows: TR = 3000 ms, TE = 40 ms, FoV = 35 × 35 mm, and MTX = 200 × 200; the parameters of the T_2 map were set as follows: TE = 6.6, 13.2, 19.8, 26.4, 33, 39.6, 46.2, 52.8, 59.4, 66, 72.6, 79.2 ms, TR = 3000 ms, and FoV = 35 mm × 35 mm.

Cytotoxicity

A Cell Counting Kit-8 (CCK-8) assay was used to evaluate the cytotoxicity of ZCISe@ZnS:Mn QDs. In brief, MCF-7 cells (iCell Bioscience Inc., Shanghai, China) were firstly seeded in a 96-well plate at a cell density of 1×10^4 cells per well, and cultured in a DMEM supplemented with 10% FBS and 1% penicillin–streptomycin solution (100×) at 37 °C under a 5% CO_2 atmosphere. Next, the cells were washed twice with 1× phosphate-buffered saline (PBS) and then incubated with the QDs of different concentrations for 24 h. Subsequently, the cells were washed three times with 1× PBS to remove free QDs and then incubated in 100 μL culture medium containing 10% CCK-8 solution at 37 °C for 1 h. Finally, the absorption of each solution at 450 nm was measured using a microplate reader (TECAN, SPARK 10M).

In vitro cellular imaging and visualization of intracellular reactive oxygen species (ROS)

MCF-7 cells were seeded in confocal culture dishes (~6×10^4 cells per dish) at 37 °C under 5% CO_2 for 24 h. Different samples (ZCISe@ZnS:Mn QDs of 2 μM, ZCISe@ZnS QDs of 2 μM, Mn^{2+} of 50 μM, or 1× PBS) were added and incubated for 2 h before irradiation (638 nm for 0 or 5 min) with a power density of 0.72 W cm^{-2}. Free samples in the culture media were removed by rinsing the cells with 1× PBS three times. After that, the cells were treated with DCFH-DA solution (0.1 mM in 1× PBS and DMSO with a solvent volume ratio of 9 : 1) for 20 min at 37 °C to facilitate ROS detection. After being rinsed two times with 1× PBS, the fluorescence imaging capacity of the cells and the intracellular levels of ROS were studied using a confocal microscope (Leica TCS SP5, Germany). The excitation was set to 514 nm. The fluorescence signal of the QDs was collected in a spectral window of 560–800 nm, and the fluorescence signal for detecting ROS was collected in a spectral window of 525–560 nm.

In vitro photodynamic evaluation of ZCISe@ZnS:Mn QDs

To assess the photodynamic efficacy *in vitro*, two staining reagents, *i.e.*, Calcein-AM and PI, were used for separately staining the live cells in green (λ_{ex} = 490 nm and λ_{em} = 515 nm) and dead cells in red (λ_{ex} = 535 nm and λ_{em} = 617 nm). MCF-7 cells were cultured in confocal culture dishes (~1×10^5 cells per dish) at 37 °C under 5% CO_2 for 24 h. The doped QDs of different concentrations were separately added to the culture dishes and further incubated for 2 h before being exposed to 638 nm light irradiation (power density of 0.72 W cm^{-2}) for 10 min. Then, 300 μL of Calcein-AM (2 μM) and PI (4.5 μM) solutions were added after the removal of the culture medium and rinsed with 1× PBS, and the cells were further cultured for

25 min. The fluorescence of the cells was observed on a confocal microscope (Leica TCS SP5, Germany).

Animal model

The subcutaneous tumor models were established upon subcutaneous injections of 4T1 cells (~5×10^6, ATCC CRL-2539) into 4-week-old female BALB/c mice at the flank region of the right hind leg. The tumor imaging studies were carried out for 5–7 d after the inoculation of tumor cells.

All animal procedures reported here were performed in accordance with the Guidelines for Care and Use of Laboratory Animals of Peking University Health Science Center, and approved by the Peking University Institutional Animal Care and Use Committee. The assigned accreditation number of the investigator is LA2022284.

Fluorescence imaging of tumors *in vivo*

The fluorescence images of mice bearing subcutaneous tumor at the right hind leg were acquired with an *in vivo* imaging system (IVIS Spectrum). In detail, the tumor-bearing mouse was anesthetized, and then the PBS (1×) solution of the QDs was intravenously injected through its tail vein (2.45 mg Cu per kg body weight). The different fluorescent channels were set by selecting the built-in filters of excitations and emissions, and the exposure time was set to 3 s. After *in vivo* imaging, the mouse was sacrificed and the main organs were extracted for *ex vivo* fluorescence imaging. The fluorescence images were analyzed with vendor software.

Multiparametric MRI of the brain *in vivo*

The brain MRI was acquired on a 7.0 T MRI scanner (Bruker BioSpec70/20 USR) equipped with a mouse head surface coil.

T_1-weighted imaging (T_1WI), T_2-weighted imaging (T_2WI), T_2*-weighted imaging (T_2*WI), and susceptibility-weighted imaging (SWI) sequences were obtained before and after intracranial injection of ~10 μL PBS solution of the QDs (0.122 mg Cu per kg). During the MRI experiments, the animals were anesthetized with 2% isoflurane in oxygen-mixed air *via* a facemask. The detailed parameters for these sequences were set as follows:

T_1WI: TR = 500 ms, TE = 5.24 ms, FoV = 22 × 22 mm, matrix = 191 × 191, and slice thickness = 0.5 mm;

T_2WI: TR = 3000 ms, TE = 40 ms, FoV = 22 × 22 mm, MTX = 191 × 191, and slice thickness = 0.5 mm;

T_2*WI: TR = 1479.31 ms, TE = 3.32 ms, FoV = 22 × 22 mm, MTX = 191 × 191, and slice thickness = 0.5 mm;

SWI: TR = 595.17 ms, TE = 7.9 ms, FoV = 22 × 22 mm, matrix = 191 × 191, and slice thickness = 0.5 mm.

Statistical analysis

Data are shown as the mean ± standard deviation, as indicated in the figure captions. Statistical differences between the two groups were determined *via* the *t*-test. A p-value < 0.05 was regarded as statistically significant. All the statistical tests were carried out using GraphPad Prism 8.0 software.

Results and discussion

Aqueous synthesis of ZCISe@ZnS:Mn QDs and doping effects

Aqueous synthesis of ZCISe@ZnS QDs was first performed according to a modified method.[31] The feed molar ratio of Zn and Cu elements was set to 1 : 7 to yield ZCISe@ZnS QDs with a high PLQY of up to 25.2%, in consideration of improving the imaging sensitivity of subsequent application. To further reduce the quenching effect of magnetic domains on the fluorescent QD core, *in situ* doping of Mn^{2+} ions with a compatible shell layer was adopted in the process of epitaxial growth of the ZnS shell. In brief, on the basis of ZCISe core QDs, the Mn precursor was simultaneously introduced along with the Zn precursor to perform doping during the ZnS shell coating. The doped QDs were denoted as ZCISe@ZnS:Mn and the Mn^{2+} doping ratio was calculated as the actual Mn^{2+} proportion of all cations within QDs. To achieve an optimal balance of the fluorescence and magnetic function of QDs, the feed doping amount of Mn^{2+} ions was varied, and the doping effects on their optical and magnetic properties were systemically investigated. The ICP-OES results in Table S1† prove that the actual Mn contents doped into the QDs are far less than their feed amounts, with the Mn^{2+} doping levels of 1.9%, 2.9%, and 9.9% corresponding to the feed proportions of 12%, 21%, and 39%, respectively. The shell growth processes were also monitored for different Mn^{2+} doping ratios. For a doping ratio of 1.9%, with the extension of the coating time of the shell, the fluorescence intensity of the QDs basically shows a gradual upward trend, which reached the maximum value at a shelling time of 5 h (Fig. S1a†). However, the strongest fluorescence for a doping ratio of 2.9% occurred at 4 h of shelling, and prolonging the reaction to 5 h resulted in a slight decrease in the PL intensity (Fig. S1b†). While for the Mn^{2+} doping ratio of 9.9%, a continuous enhancement of PL was observed along with the reaction time, suggesting that manganese is successfully doped with the QDs *via* a shell growth doping strategy, which is consistent with the case for previously reported Mn-doped $CuInSe_2$@ZnS QDs.[25] Importantly, a gradual red-shift of the PL profile (Fig. S1c†) can be clearly observed along with the doping process for a Mn^{2+} doping ratio of 9.9%.

Fig. 1a and 1b clearly show the gradual decrease of PL intensity and red-shift of the emission along with the increase of the Mn^{2+} doping ratio for all the QDs with a shell growth time of 5 h. The PLQY decreased from an initial 25.2% for undoped QDs to 18.9% for a doping ratio of 9.9%. Nevertheless, this fluorescence quantum yield still ranks at the top of those for aqueously prepared Cd-free QDs at similar emission wavelengths (~780 nm),[46–49] as shown in Table S2.† It should also be mentioned that the decrease of PL intensity caused by the Mn^{2+} dopant is relatively not significant compared with those cases for doping magnetic ions into QD cores,[50,51] suggesting the important role of the ZnS shell as a spacer between the underlying ZCISe core and the dopant to boost the PLQY. The observed red-shift of the emission peak wavelength from 750 nm to 778 nm after successful Mn^{2+} doping is consistent with previous reports, which can be attrib-

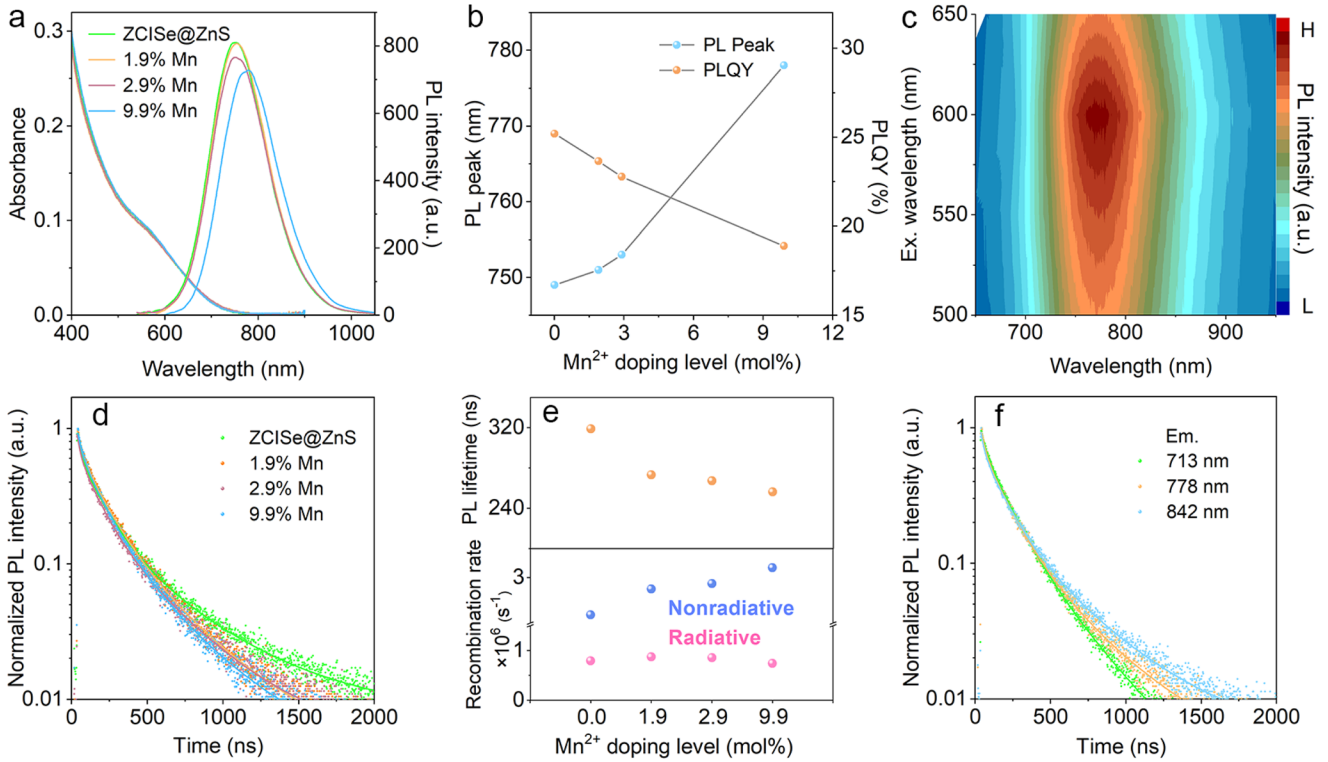

Fig. 1 (a) PL and absorption spectra of ZCISe@ZnS:Mn QDs with different Mn^{2+} doping levels, (b) the evolution of the PL peak and PLQY of the QDs against the Mn^{2+} doping level, (c) PL spectra recorded by excitation at different wavelengths for ZCISe@ZnS:Mn QDs with a Mn^{2+} doping level of 9.9%, (d) time-resolved PL decay curves of ZCISe@ZnS:Mn QDs with different Mn^{2+} doping levels, (e) the average lifetime and non-radiative/radiative recombination rates as a function of the Mn^{2+} doping level, and (f) time-resolved PL decay curves of ZCISe@ZnS:Mn QDs with a Mn^{2+} doping level of 9.9% at different emission wavelengths.

uted to the interaction between the 3d electrons of Mn^{2+} and charge carriers in the conduction/valence band.[52] Moreover, the doping did not change the nature of broad excitation (400–700 nm) and excitation-independent emission of ZCISe@ZnS QDs as shown in Fig. 1c and Fig. S2,† providing great flexibility in the choice of excitation light sources for practical applications.

To understand the Mn^{2+} doping effects on the photoluminescence process, the charge carrier recombination kinetics of doped QDs as a function of the Mn^{2+} doping level was further studied by time-resolve PL measurements. The PL decay curves determined at their corresponding PL peak wavelengths are shown in Fig. 1d. In general, all QDs have PL relaxations characterized by multiexponential decay processes. Their best fits were obtained by three exponential functions, which are summarized in Table S3.† The calculated average PL lifetimes are generally long (>250 ns). For the Mn-doped QDs, it is obvious that the average lifetimes show a strong dependence on the Mn^{2+} doping levels. Along with the increase in the Mn^{2+} doping ratio, the average lifetime exhibits a sharp decline from the initial 319 ns and then gradually decreases to 256 ns as shown in the upper panel of Fig. 1e. The apparently lowered lifetime is mainly caused by the acceleration of the slowest decay channel (from initial 490 ns for undoped QDs to 394 ns for 9.9% of the Mn^{2+} doping level), while the recombination rates of the other two channels remain nearly unchanged. The slowest decay channel is largely related to the donor–acceptor pair (DAP) recombination,[25,27] which finds support from the emission wavelength-dependent PL lifetime of the QDs with a Mn^{2+} doping ratio of 9.9% (Fig. 1f and Table S4†), and this dependence was also observed for undoped QDs (Fig. S3 and Table S5†). In principle, the introduction of dopants into the QD lattice could inevitably create new Mn^{2+}-related defects, especially considering that Mn^{2+} doping started simultaneously with ZnS shell coating across the core/shell interfaces. In this case, the doped Mn^{2+} ions could affect the charge carrier recombination process through newly formed defect states associated with interfacial Mn^{2+} dopants in the ZnS shell, leading to the decreased PLQY value, as evidenced by an apparent increase of the non-radiative recombination rate as a function of the Mn^{2+} doping level (the lower panel of Fig. 1e).

In order to study the effects of Mn^{2+} doping on the structure of ZCISe@ZnS QDs, TEM analysis combined with XRD was carried out. As shown in Fig. 2a–c, the morphology and monodispersity of the QDs exhibit no obvious change after 9.9% of Mn^{2+} doping, with an average particle size of about 3.0 nm. The XRD patterns of all QDs in Fig. 2d match well with the tetragonal crystal phase of $CuInSe_2$ QDs (JCPDS card no. 40-1487), which are consistent with the HRTEM results

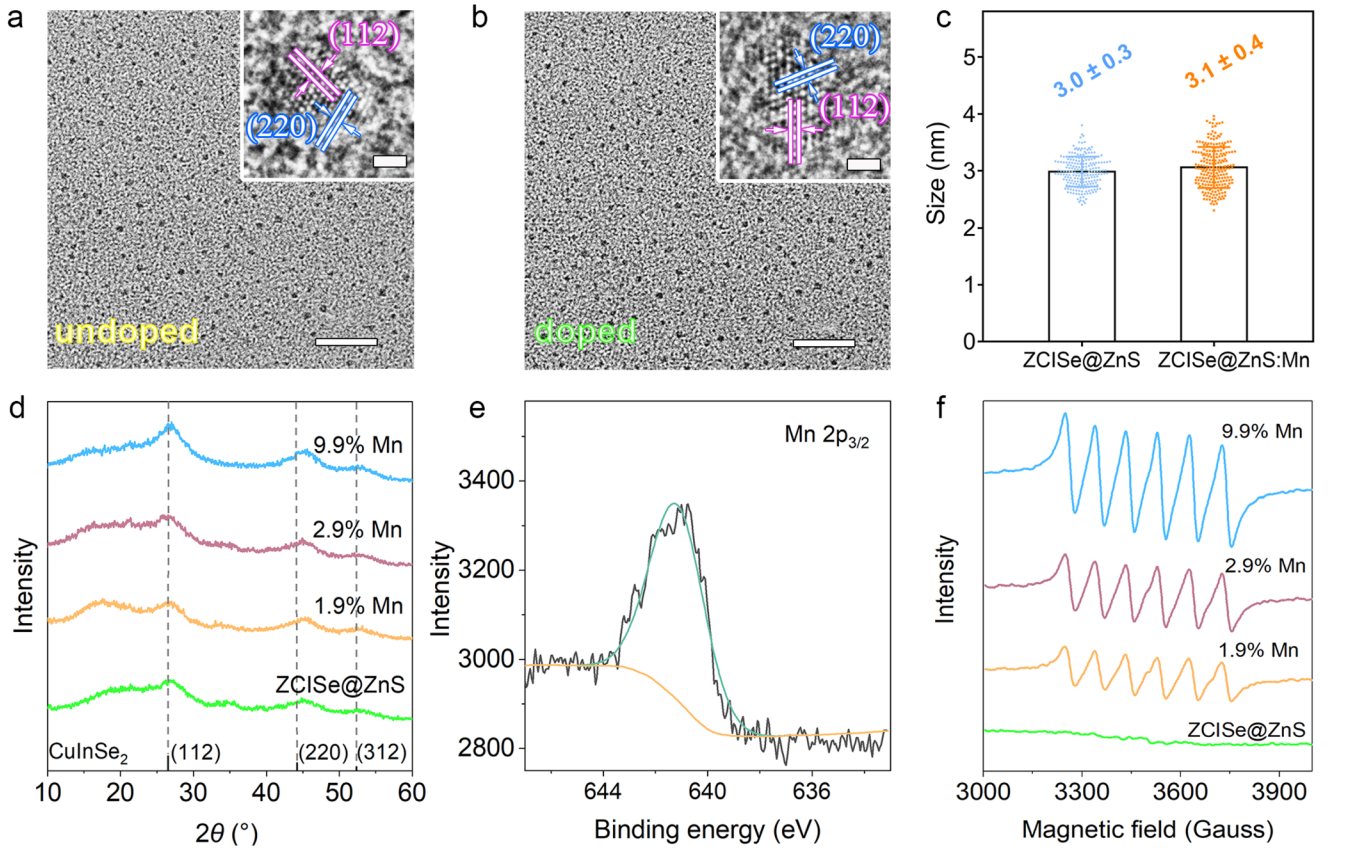

Fig. 2 TEM images of ZCISe@ZnS QDs (a) and ZCISe@ZnS:Mn (doping level of 9.9%) QDs (b) with the insets showing the HRTEM images of the corresponding QDs (the scale bars for TEM and HRTEM are 20 nm and 1 nm, respectively), (c) the size histograms of two QDs, (d) powder XRD patterns of ZCISe@ZnS:Mn QDs with different Mn^{2+} doping levels together with the line pattern for tetragonal $CuInSe_2$ (black line, JCPDS 40-1487), (e) high-resolution XPS spectrum of Mn element for ZCISe@ZnS:Mn QDs with a Mn^{2+} doping level of 9.9%, and (f) EPR spectra of ZCISe@ZnS:Mn QDs with different Mn^{2+} doping levels.

shown in the insets of Fig. 2a and 2b. In particular, for Mn-doped QDs, the diffraction peaks at about 44° show a slight shift towards a larger angle. This might be due to that the interdiffusion of Zn^{2+} and Mn^{2+} ions to the core of the QDs results in the lattice shrinkage,[51] since the ion radii of Zn^{2+} (74 pm) and Mn^{2+} (70 pm) were smaller than those of In^{3+} (80 pm) and Cu^{+} (77 pm).[53] These results further demonstrate the successful doping of the Mn element into ZCISe@ZnS QDs.

XPS was performed to identify the valence state of the Mn element in the QDs, and Fig. 2e clearly displays the characteristic peak of the Mn $2p_{3/2}$ signal appearing at 641.6 eV, demonstrating that the dopants are in the Mn(II) state. The results shown in Fig. S4† also confirm the gradual incorporation of the Mn element into the QDs and the valence state of Cu within the QDs to be Cu(I). The EPR spectra for QDs of increasing Mn^{2+} doping levels are given in Fig. 2f, which were characterized by a six-line hyperfine splitting pattern appearing for all the levels of Mn^{2+} doping (with the g value in a range of 2.003–2.007). In contrast, only a background signal was observed for undoped QDs. The six-line patterns belong to the signature of the electron-nuclear hyperfine coupling of Mn^{2+} (nuclear spin I = 5/2).[54] The EPR results demonstrate that Mn^{2+} ions were successfully incorporated into the ZnS shell. Compared with broad EPR resonances without splitting reported for Mn-doped $CuIn(S,Se)_2$-based QDs,[25,52] which may be due to the formation of manganese clusters, the current results are more consistent with the case for $CdSe/Zn_{1-x}Mn_xS$ nanoparticles, where Mn^{2+} ions tend to be doped homogeneously into the ZnS shell lattice by facilely substituting Zn^{2+}.[54,55] Furthermore, the relatively high hyperfine splitting constant A values of about 90×10^{-4} cm^{-1} are similar to those for Mn-doped CdTe/ZnS QDs reported previously,[54] indicating that the isolated Mn^{2+} ions appear to locate near the surface of the thin ZnS shell of the QDs.

In vitro evaluation of cytotoxicity, MR contrast enhancement effect, fluorescence imaging capability, and photodynamic efficacy of ZCISe@ZnS:Mn QDs

Based on the ZCISe@ZnS:Mn QDs with intrinsic NIR fluorescence and magnetic properties, their temporal stabilities desirable for practical applications were first evaluated *in vitro*. Long-term monitoring of PL proves that all QDs possess stable fluorescence within one month (Fig. 3a), providing both the essential fluorescence and colloidal stability needed for giving

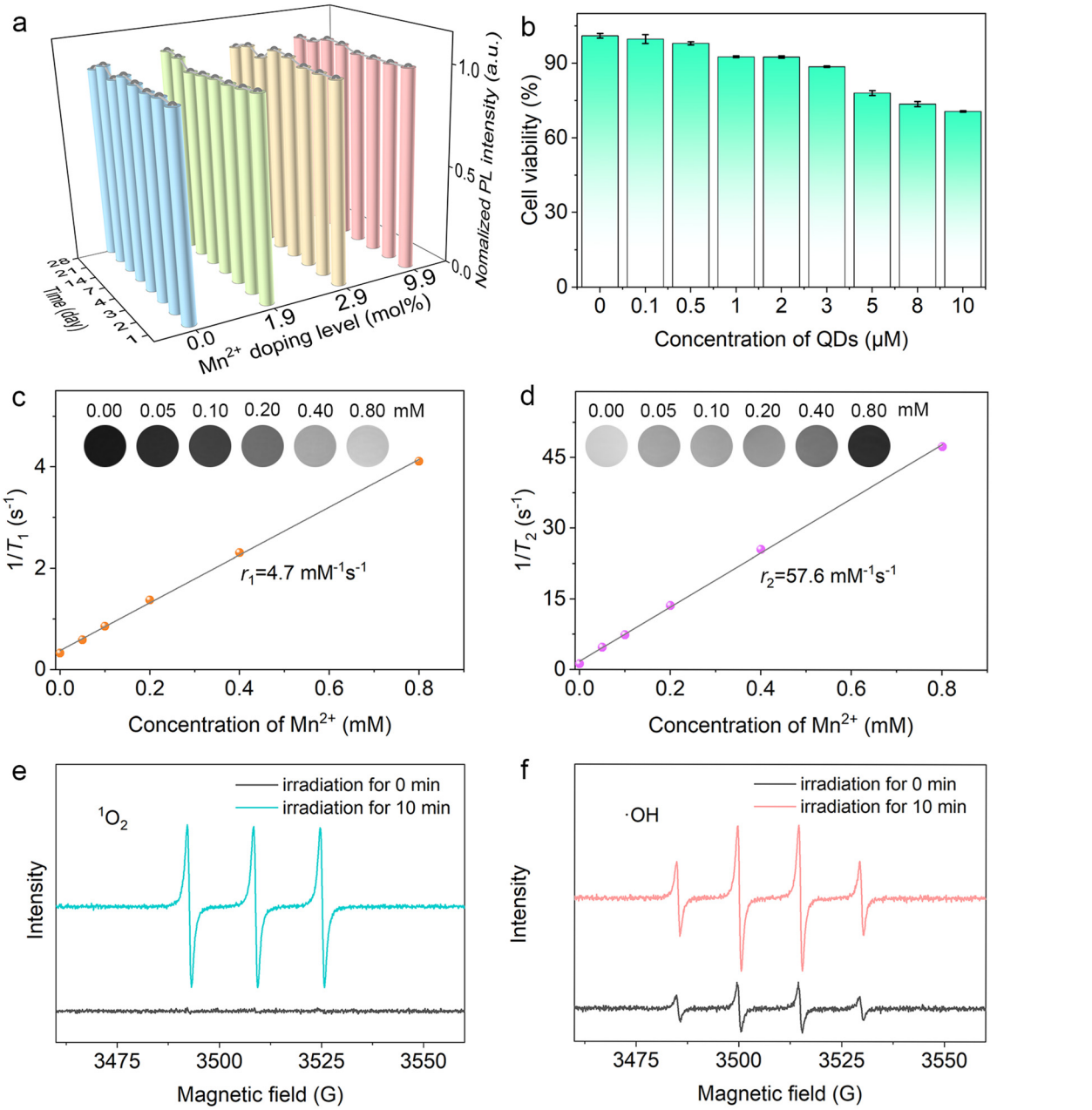

Fig. 3 (a) Temporal evolutions of PL intensity of ZCISe@ZnS:Mn QDs with different Mn^{2+} doping levels, (b) cell viability of MCF-7 cells recorded after being treated with ZCISe@ZnS:Mn (doping level of 9.9%) QDs, the longitudinal relaxation rate (c) and transverse relaxation rate (d) against the concentration of Mn^{2+} in doped QDs with the MR contrast images of aqueous solutions containing QDs (doping level of 9.9%) shown in the insets, and EPR spectra of ZCISe@ZnS:Mn (doping level of 9.9%) QDs for detecting $^1O_2$ (e) and ·OH (f) with or without light irradiation (638 nm, 0.72 W cm^{-2}).

reliable signals. The cytotoxicity of the QDs with a Mn^{2+} doping level of 9.9% was evaluated using the CCK-8 assay. The results in Fig. 3b show that the cell survival rate can be maintained above 70% at a QD concentration of up to 10 μM, which is about 1.5-fold higher than the dose used for subsequent *in vivo* imaging studies (2.45 mg Cu per kg body weight). This manifests the potential biocompatibility and biosafety of ZCISe@ZnS:Mn QDs for *in vivo* application.

Since the doped Mn^{2+} ions within the QDs can affect the MRI signals of nuclear longitudinal relaxation of water protons as paramagnetic centers, the current QDs are expected to show great potential for MRI application. In order to evaluate the capability of the doped QDs to shorten the longitudinal relaxation time (T_1) and transverse relaxation time (T_2) of water protons, the relaxivities of the QDs with a Mn^{2+} doping level of 9.9% were determined using a 7.0 T MRI scanner as described in the Experimental section in detail. As shown in Fig. 3c and 3d, the QDs show significant T_1 and T_2 MR contrast enhancement effects, with a remarkable increase of concentration-dependent longitudinal relaxation rate ($1/T_1$) and transverse

relaxation rate ($1/T_2$). Through linear fitting, the molar longitudinal relaxivity r_1 and transverse relaxivity r_2 can be extracted to be 4.7 and 57.6 mM^{-1} s^{-1}, respectively. According to the origin of T_1 enhancement, the longitudinal relaxivity of water protons involved in the inner sphere can be enhanced by slowing the tumbling of the paramagnetic Mn^{2+} dopants distributed near the shell surface.[54,56] Surprisingly, the transverse relaxivity of water protons was also increased simultaneously by Mn-doped QDs, integrating dual T_1 and T_2 contrast enhancements into one QD. Such optimization of the relaxometric properties favors the rational design of multiparametric MRI contrast agents.

In addition to the above magnetic properties, in order to evaluate the generation ability of reactive oxygen species (ROS) from the Mn-doped QDs, EPR measurements were conducted to distinguish the possible ROS qualitatively. Here, 100 μM of H_2O_2 was used for EPR tests to simulate those existing within the tumor microenvironment. As shown in Fig. 3e and 3f, both $^1O_2$ and ·OH were largely generated in the presence of Mn-doped QDs and light irradiation (638 nm for 10 min, 0.72 W cm^{-2}). In contrast, the lack of irradiation only yielded quite limited ·OH, suggesting that the current QDs have the potential to kill tumor cells through the generation of excessive ROS when activated by light.

Next, the fluorescence imaging capability and photodynamic efficacy of ZCISe@ZnS:Mn QDs were evaluated on MCF-7 cells. The cells incubated with free Mn^{2+} ions and ZCISe@ZnS QDs were used as control groups. As shown in Fig. 4a, the confocal fluorescence microscopy images acquired under a red channel (560–800 nm) reveal that the cells treated with the QDs show a strong red fluorescence signal of QDs, while those incubated with free Mn^{2+} ions exhibit nearly no

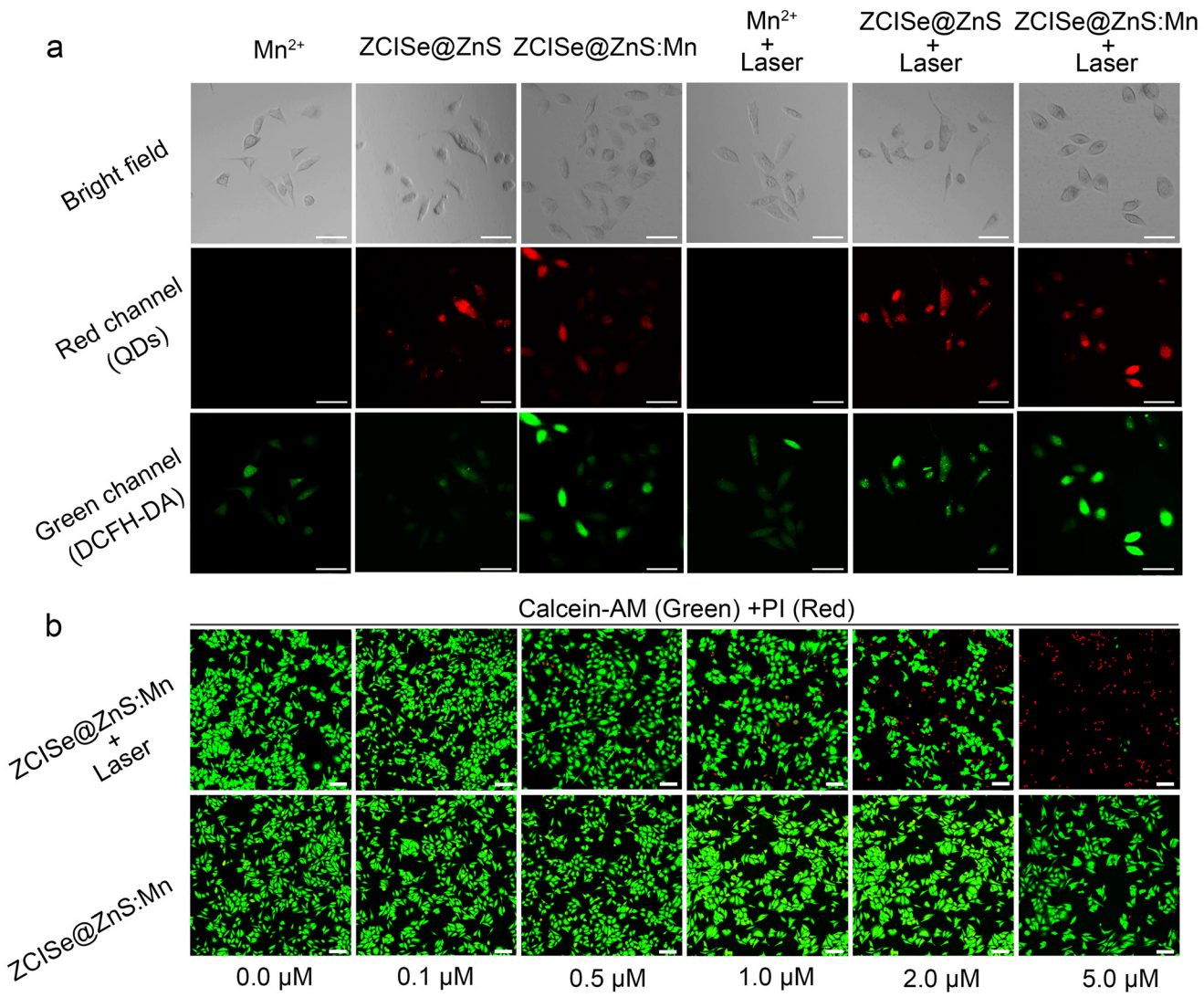

Fig. 4 (a) Bright field and confocal fluorescence images of MCF-7 cells treated with different samples with or without light irradiation, and (b) confocal fluorescence images of MCF-7 cells treated with ZCISe@ZnS and ZCISe@ZnS:Mn QDs of different concentrations, respectively, followed by live–dead cell staining. The scale bars in panels (a and b) correspond to 75 and 100 μm, respectively.

fluorescence signal under the same conditions. This result suggests that the current QDs can be ingested by cancer cells. Since the Mn^{2+} doping did not largely lower the PLQY of the QDs, the fluorescence signal intensities of the cells show no distinct difference for doped and undoped QDs. In particular, upon 638 nm light irradiation for 5 min, the fluorescence

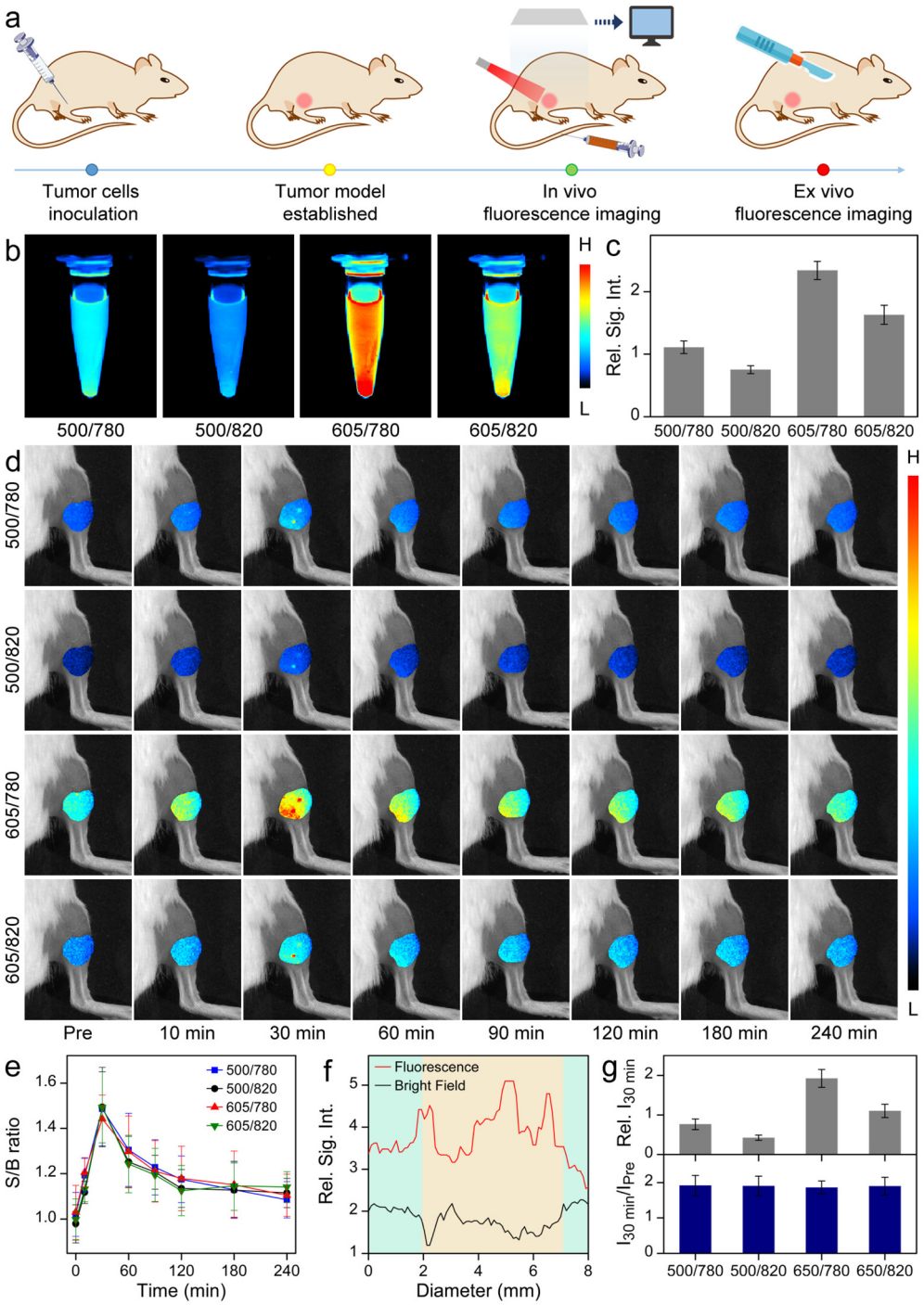

Fig. 5 (a) Schematic illustration of the tumor imaging procedures, (b) multi-channel fluorescence images of PBS solution of QDs, together with the (c) quantitative analysis of the corresponding relative signal intensities, (d) *in vivo* multi-channel fluorescence images of subcutaneous tumors recorded before and at different time points after intravenous injection of the QDs, together with the (e) corresponding temporal evolution of the signal to background (S/B) ratio calculated by the signal intensity ratio of tumor sites to surrounding tissues, (f) line-scanning spectra drawn across the tumor region in the λ_{ex} 605/λ_{em} 780 channel fluorescence image and bright field image, and (g) upper: the relative signal intensities of tumor region at different channels recorded at 30 min post-injection of the QDs (I_{30min}), and lower: the ratio of the fluorescence signal intensity of tumor region at 30 min post-injection (I_{30min}) to pre-injection of the QDs (I_{pre}).

signals of cancer cells show no obvious decline, manifesting the high stability of the QDs.

For visualizing the intracellular ROS, all cells were treated with DCFH-DA before imaging under a green channel (525–560 nm). As shown in the third row of Fig. 4a, fluorescence signals can be observed for the cells treated with free Mn^{2+} ions, indicating that Mn^{2+} ions can convert a certain amount of endogenous H_2O_2 into ROS through Fenton-like reactions inside the cells, which is similar to the case for applying the Fenton-like activity of Mn^{2+} ions to generate ·OH from H_2O_2.[57,58] In contrast, the cells treated with PBS show no fluorescence signal (Fig. S5†). The undoped QDs also led to a certain degree of green fluorescence, which may be attributed to the radicals transformed from the photoexcited charge carriers during the non-radiative recombination processes of ZCISe@ZnS QDs. Interestingly, for the Mn-doped QDs, the fluorescence of the cells is significantly enhanced, largely due to the synergistic effect of the Fenton-like activity of doped Mn^{2+} ions distributed near the surface of the thin ZnS shell and photodynamic process of the QDs for boosting the production of ROS. To prove whether light irradiation can enhance the above two pathways, the cells were further treated with the same three samples under 638 nm light irradiation for 5 min. Free Mn^{2+} ions show no apparent enhancement of the ROS yield, suggesting that the Fenton-like activity of free Mn^{2+} ions did not change much under the current irradiation conditions. The fluorescence signals caused by the undoped QDs show an obvious increase because light irradiation can give rise to more radicals through non-radiative relaxations. Quite excitingly, the cells treated with the Mn-doped QDs exhibit further enhanced fluorescence after light irradiation, demonstrating that light can promote both the nonradiative recombination of the QD core and doped Mn^{2+} ion-associated Fenton-like reactions and thus yield more ROS. This might involve photo-assisted Fenton reactions as previously reported for a $Cu_{2-x}Se$ nanoparticle-based system for effectively producing ROS.[59] Overall, the Mn-doped ZCISe@ZnS QDs can combine chemodynamic and photodynamic processes for effectively yielding ROS to achieve great potential for killing cancer cells.

To assess the photodynamic efficacy *in vitro*, the viabilities of MCF-7 cells after being treated with ZCISe@ZnS:Mn QDs of different concentrations were studied. Calcein-AM and PI costainings were adopted to distinguish live and dead cells. As shown in Fig. 4b, the Mn-doped QDs under irradiation at 638 nm (0.72 W cm^{-2} for 10 min) resulted in a gradual increase of dead cells (red) when the QD concentration reached above 0.5 μM, and most cells were killed by the QDs with a concentration up to 5 μM in the presence of light irradiation. In contrast, the number of dead cells treated with the QDs without laser irradiation is far smaller. Therefore, ZCISe@ZnS:Mn QDs can efficiently kill MCF-7 cells upon light irradiation, showing favorable properties for photodynamic therapy.

Multi-channel NIR fluorescence imaging of tumors *in vivo*

On the basis of the strong NIR emissive property of the current Mn-doped QDs, the tumor diagnosis capacity of the QDs was further investigated *in vivo* in a rodent animal model. The detailed procedures of the imaging experiment are illustrated in Fig. 5a. Owing to the complicated physiological and pathological environment of the solid tumor, the single-channel fluorescent signal is easily affected by the background fluorescent signals of endogenous biomolecules whose maximum excitations and emissions are similar to the selected conditions, thereby reducing the accuracy of tumor detection. In this context, multi-channel optical tumor detection is important for avoiding false positives, allowing for a better diagnosis of the tumors. Benefiting from the broad excitation and appropriate NIR emission profiles of the current QDs, the solid tumor of the mouse is expected to be detected by multiplexed fluorescence channels.

As a proof of concept, four different fluorescence channels, *i.e.*, λ_{ex} 500/λ_{em} 780, λ_{ex} 500/λ_{em} 820, λ_{ex} 605/λ_{em} 780, and λ_{ex} 605/λ_{em} 820, were selected to jointly image the solid tumors. Before the *in vivo* experiment, the multi-channel imaging performance of the QD solution was first evaluated on the imaging equipment. As presented in Fig. 5b, the multi-channel fluorescence images of QD PBS solutions in the Eppendorf tube were acquired. The QD solution shows strong fluorescence signals in all four channels but with different intensities. Specifically, QDs can be excited by both 500 nm and 605 nm lasers to emit bright NIR light peaked at the wavelengths of 780 nm and 820 nm respectively, which exhibited the strongest fluorescence in the λ_{ex} 605/λ_{em} 780 channel. This optical performance of QD solution in different fluorescence channels can also be confirmed by the quantitative analysis of fluorescence intensity values, as shown in Fig. 5c. These data imply that the current QDs possess the potential to detect tumors *in vivo* through all these fluorescence channels.

To confirm this expectation, a mouse bearing subcutaneous tumor was adopted to validate the tumor-specific imaging performance of the QDs *in vivo*. The PBS solution of the QDs with a dose of 2.45 mg Cu per kg body weight was intravenously administered into the mouse through its caudal vein. The fluorescence images of the right hind leg of the mouse were acquired before and at different time points after the injection of the QDs. As shown in Fig. 5d, after the QDs were delivered intravenously, the NIR fluorescence signals at the tumor site became apparent 10 min after injection. Thereafter, the signals of the tumor region quickly increased in intensity and reached a maximum at approximately 30 min post-injection in all fluorescence channels, suggesting that the QDs are stable in a physiological environment and can specifically accumulate in the tumor tissue, allowing the multi-channel diagnosis of the tumors *in vivo*. Through the quantitative analysis of the fluorescence signal intensities derived from tumor and the surrounding tissues, the temporal evolution of the signal-to-background ratio of the tumor region exhibited a roughly similar tendency. These results indicate that although the fluorescence signal intensities of tumor vary among these four different channels, the location of solid tumor can be distinguished in all these channels, in which the tumor tissue exhibited a ~1.5 times higher signal

intensity than the surrounding tissues at 30 min post-injection (Fig. 5e).

In order to better show the tumor imaging performance of the current QDs, the line-scanning spectra drawn across the tumor region in a bright field image and a λ_{ex} 605/λ_{em} 780 channel fluorescence image were obtained, as a proof of concept. As presented in Fig. 5f, the background of the curve image was set to light yellow and green to distinguish the tumor segment and the tissue segment. Interestingly, these two curves showed a symmetrical opposite trend. On one hand, owing to the angiogenesis and tissue denaturation, the skin on the grafting tumor exhibited a darker color compared with the surrounding normal skin in the gray image of the bright field, indicated by the low signal values of the tumor segment of the bright field curve. On the other hand, the tumor segment of the fluorescence curve exhibited a significant increase of the signal intensity value compared to the tissue segments on both sides, suggesting that the fluorescent signal of tumor is specifically enhanced by the QDs. In addition, the signal enhancement at the junction of tumor and tissue segments is very sharp, indicating that the tumor margin can be well identified. The symmetrically opposite trend of these two curves confirms the co-localization of enhanced fluorescence signals and tumor region. These above results indicate that the tumor region can be precisely identified by QD-based tumor imaging, with high spatial resolution.

For further validating the tumor contrast enhancement of the QDs, the relative signal intensities of tumor at pre-injection and 30 min post-injection were recorded. As shown in the upper panel of Fig. 5g, through quantitative analysis, the relative signal intensity trend of the tumor region *in vivo* is consistent with that of QD solution in Eppendorf tubes in four different channels as shown in Fig. 5b. However, even if the fluorescent signal intensities of tumor were distinct in different channels, the intensity ratios at 30 min post-injection to pre-injection in these imaging channels are almost identical, *i.e.*, the tumor contrast was enhanced by ~1.9 times after 30 min injection of QDs in all imaging channels.

To further confirm the tumor accumulation of the QDs, the main organs including the heart, liver, spleen, lung, kidney,

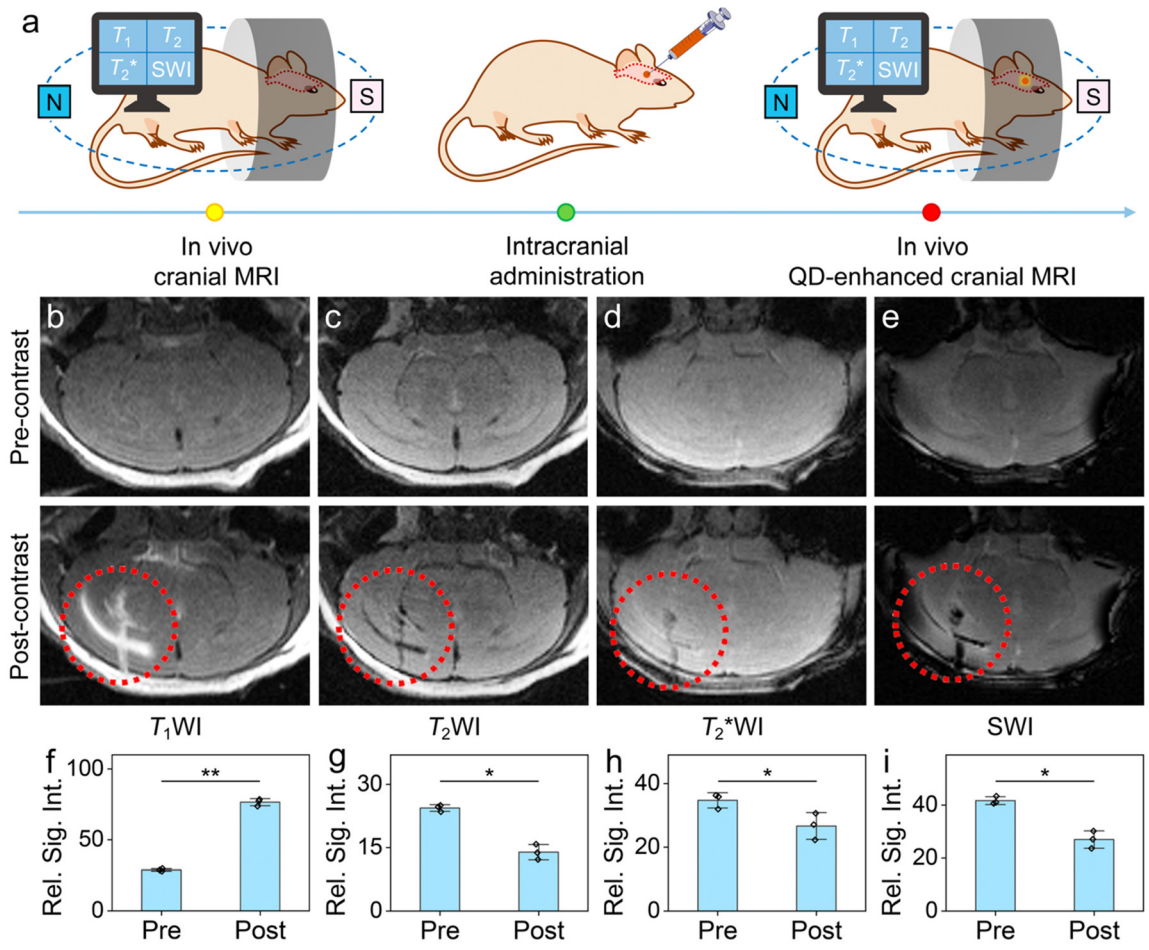

Fig. 6 (a) Schematic illustration of the cranial MRI procedure, (b) T_1WI, (c) T_2WI, (d) T_2*WI, and (e) SWI of the mouse brain recorded before (upper) and after (lower) intracranial injection of the QDs, and (f–i) the average relative signal intensities (Rel. Sig. Int.) of QD accumulation regions in the mouse brain after QD injection (post) and the corresponding brain regions before injection (pre). Data are shown as mean ± SD (3 imaging planes). Statistical significance was determined by paired *t*-test (*p < 0.05 and **p < 0.01).

and tumor were harvested, and subjected to *ex vivo* fluorescence imaging. As shown in Fig. S6,† the *ex vivo* tumor tissue of the mouse at the λ_{ex} 605/λ_{em} 780 channel still exhibited an obvious fluorescence signal even if the fluorescence signal of tumor has been greatly faded at 4 h post-injection in the *in vivo* imaging, and this result supports the excellent tumor retention properties of the current QDs.

Multiparametric MR imaging of the brain *in vivo*

Encouraged by the considerable T_1 and T_2 MR contrast enhancement effects, the current QDs are further expected to serve as versatile contrast agents for different MRI sequences, for realizing the enhanced multiparametric MRI. In order to evaluate the *in vivo* MRI performance of the QDs, BALB/c mice were adopted as the animal model, and the PBS solution of the QDs was intracranially injected into the mouse brain with a dosage of 0.122 mg Cu per kg body weight. The cranial MR images of mice were acquired before and after injection of the QDs, respectively, on a 7.0 T animal MRI scanner.

To investigate the contrast enhancement performance of the QDs in multiparametric MRI, different MRI sequences were selected to simultaneously show the brain section of the mice. The detailed procedures are given in Fig. 6a. In the clinic, T_1WI and T_2WI have been widely employed as the basic MRI sequences to reveal the anatomical structure of the brain. As shown in Fig. 6b and 6c, the image contrast between different encephalic regions is not obvious before the intracranial injection of the QDs, only the boundary of hippocampus is vaguely visible in T_2WI. In contrast, after intracranial injection of the QDs, significant signal enhancements appeared inside the brain. Specifically, a bright signal and a dark signal can be observed around the injection needle track and injection point in T_1WI and T_2WI, respectively. In addition, the bright/dark signals were also distributed in the lateral ventricle at the edge of the alveus of the hippocampus, which largely enhanced the contrast of the boundary between the hippocampus and cortex, suggesting that the QDs may diffuse into the lateral ventricle through the needle track. Apparently, the signals with the same spatial distribution but opposite trends in T_1WI and T_2WI indicate that the QDs can simultaneously serve as positive and negative contrast agents in these two MRI sequences.

In addition to T_1WI and T_2WI, T_2*WI and SWI, two gradient-recalled-echo sequences of MRI that have been used for detecting brain micro-bleeding in the clinic, were also adopted for brain imaging. As shown in Fig. 6d and 6e, the negative enhancement signals can be clearly observed in both T_2*WI and SWI after the intracranial injection of the QDs. More importantly, the spatial distribution of the negative signals in these two MRI sequences matched well with that of the aforementioned enhanced signals in T_1WI and T_2WI, indicating that these negative signals are attributed to the injected QDs. These results indicate that the current QDs can serve as the multiparametric MRI contrast agents for T_1WI, T_2WI, T_2*WI, and SWI.

In order to further evaluate the enhancement of the imaging contrast by the QDs in different MRI sequences, the signal intensities in the above MR images were quantitatively analyzed. In detail, the signal intensities of the QD accumulation regions in the mouse brain after injection and the corresponding brain regions before injection were recorded, respectively. According to the paired *t*-test statistics of signal intensities derived from three imaging planes of each MRI sequence (Fig. 6f–i), the average signal intensities of the QD accumulation area post-injection and the corresponding area pre-injection are statistically different ($p < 0.05$), indicating that the injected QDs can bring significant tissue contrast enhancement for multiparametric MRI.

Therefore, the current QDs can significantly enhance the imaging contrast of local brain tissues *in vivo* with different MRI sequences including T_1WI, T_2WI, T_2*WI and SWI, realizing the contrast enhanced multiparametric MRI of the brain.

Conclusions

In summary, we have demonstrated a multifunctional QD nanoplatform with built-in NIR photofunction and magnetic domains. By leveraging the Mn^{2+} doping kinetics in the aqueous synthetic system, magnetically engineered Zn–Cu–In–Se@ZnS:Mn core@(doped) shell QDs were achieved, further balancing the NIR fluorescence and magnetic property. The bright NIR-emitting QDs with a broad excitation range were delicately applied for the precise visualization of tumors *in vivo* using a murine breast cancer model. In addition, the doped QDs exhibit dual-modal MR contrast enhancement effects, with high molar longitudinal relaxivity r_1 and transverse relaxivity r_2 of 4.7 and 57.6 mM^{-1} s^{-1}, respectively. Encouraged by this, multiparametric MR imaging of the brain has been successfully demonstrated *in vivo*. Moreover, the generated ROS by non-radiative recombination pathways of the current Mn-doped QDs upon light irradiation were fully utilized to kill tumor cells, in combination with the chemodynamic conversion of endogenous H_2O_2 within the tumor cells to ROS based on the shell-doped Mn^{2+} ion-involved Fenton-like reactions. These investigations on the reliable construction of built-in multifunctionality in QDs may shed light on the possible mechanisms of manganese-doped photoactive nanomaterials for photo-assisted disease theranostics.

Conflicts of interest

There are no conflicts to declare.

Acknowledgements

The authors acknowledge the financial support from the National Natural Science Foundation of China (NSFC) (22177115, 82102679, 21802083), the Natural Science Foundation of Shandong Province of China (ZR2023MB057), the National Key Research and Development Program of China

(2018YFA0208800), and the Youth Innovation Promotion Association CAS (Y2022017).

References

1 L. Liu, B. Bai, X. Yang, Z. Du and G. Jia, *Chem. Rev.*, 2023, **123**, 3625–3692.
2 Y. Zhong, Z. Ma, F. Wang, X. Wang, Y. Yang, Y. Liu, X. Zhao, J. Li, H. Du, M. Zhang, Q. Cui, S. Zhu, Q. Sun, H. Wan, Y. Tian, Q. Liu, W. Wang, K. C. Garcia and H. Dai, *Nat. Biotechnol.*, 2019, **37**, 1322–1331.
3 S. Ling, X. Yang, C. Li, Y. Zhang, H. Yang, G. Chen and Q. Wang, *Angew. Chem., Int. Ed.*, 2020, **59**, 7219–7223.
4 J. Li and K. Pu, *Chem. Soc. Rev.*, 2019, **48**, 38–71.
5 Q. Chen, C. Li and Q. Wang, *Small Methods*, 2023, **7**, 2201457.
6 H. Dai, Q. Shen, J. Shao, W. Wang, F. Gao and X. Dong, *Innovation*, 2021, **2**, 100082.
7 K. J. McHugh, L. Jing, S. Severt, M. Cruz, M. Sarmadi, H. Jayawardena, C. Perkinson, F. Larusson, S. Rose, S. Tomasic, T. Graf, S. Tzeng, J. Sugarman, D. Vlasic, M. Peters, N. Peterson, L. Wood, W. Tang, J. Yeom, J. Collins, P. Welkhoff, A. Karchin, M. Tse, M. Gao, M. Bawendi, R. Langer and A. Jaklenec, *Sci. Transl. Med.*, 2019, **11**, eaay7162.
8 G. Lv, W. Guo, W. Zhang, T. Zhang, S. Li, S. Chen, A. S. Eltahan, D. Wang, Y. Wang, J. Zhang, P. C. Wang, J. Chang and X.-J. Liang, *ACS Nano*, 2016, **10**, 9637–9645.
9 W. Lian, D. Tu, P. Hu, X. Song, Z. Gong, T. Chen, J. Song, Z. Chen and X. Chen, *Nano Today*, 2020, **35**, 100943.
10 F. P. García de Arquer, D. V. Talapin, V. I. Klimov, Y. Arakawa, M. Bayer and E. H. Sargent, *Science*, 2021, **373**, eaaz8541.
11 X. Xie, J. Zhao, O. Lin, Z. Yin, X. Li, Y. Zhang and A. Tang, *J. Phys. Chem. Lett.*, 2022, **13**, 11857–11863.
12 Z. Liu, Z. Guan, X. Li, A. Tang and F. Teng, *Adv. Opt. Mater.*, 2020, **8**, 1901555.
13 X.-g. Wu, H. Ji, X. Yan and H. Zhong, *Nat. Nanotechnol.*, 2022, **17**, 813–816.
14 B. Chen, N. Pradhan and H. Zhong, *J. Phys. Chem. Lett.*, 2018, **9**, 435–445.
15 H. Song, Y. Lin, M. Zhou, H. Rao, Z. Pan and X. Zhong, *Angew. Chem., Int. Ed.*, 2021, **60**, 6137–6144.
16 A. Bora, A. Prudnikau, N. Fu, R. Hübner, K. B. L. Borchert, D. Schwarz, N. Gaponik and V. Lesnyak, *Chem. Mater.*, 2022, **34**, 9251–9260.
17 J. F. L. Lox, Z. Dang, V. M. Dzhagan, D. Spittel, B. Martín-García, I. Moreels, D. R. T. Zahn and V. Lesnyak, *Chem. Mater.*, 2018, **30**, 2607–2617.
18 L. Cao, X. Jia, W. Gan, C.-G. Ma, J. Zhang, B. Lou and J. Wang, *Adv. Opt. Mater.*, 2023, **33**, 2212135.
19 J. Ning, Z. Duan, S. V. Kershaw and A. L. Rogach, *ACS Nano*, 2020, **14**, 11799–11808.
20 Y. Zhan, S. Ling, H. Huang, Y. Zhang, G. Chen, S. Huang, C. Li, W. Guo and Q. Wang, *Angew. Chem., Int. Ed.*, 2021, **60**, 2637–2642.
21 W. Zhang, T. Chen, L. Su, X. Ge, X. Chen, J. Song and H. Yang, *Anal. Chem.*, 2020, **92**, 6094–6102.
22 Y. Zhou, B. Huang, S.-H. Chen, S.-L. Liu, M. Zhang and R. Cui, *Nano Res.*, 2023, **16**, 2719–2727.
23 B. Huang, T. Tang, S.-H. Chen, H. Li, Z.-J. Sun, Z.-L. Zhang, M. Zhang and R. Cui, *Nat. Commun.*, 2023, **14**, 197.
24 Z. Hu, C. Fang, B. Li, Z. Zhang, C. Cao, M. Cai, S. Su, X. Sun, X. Shi, C. Li, T. Zhou, Y. Zhang, C. Chi, P. He, X. Xia, Y. Chen, S. S. Gambhir, Z. Cheng and J. Tian, *Nat. Biomed. Eng.*, 2020, **4**, 259–271.
25 Y. Li, P. Zhang, W. Tang, K. J. McHugh, S. V. Kershaw, M. Jiao, X. Huang, S. Kalytchuk, C. F. Perkinson, S. Yue, Y. Qiao, L. Zhu, L. Jing, M. Gao and B. Han, *ACS Nano*, 2022, **16**, 8076–8094.
26 L.-L. Chen, L. Zhao, Z.-G. Wang, S.-L. Liu and D.-W. Pang, *Small*, 2021, **18**, 2104567.
27 M. Jiao, A. S. Portniagin, X. Luo, L. Jing, B. Han and A. L. Rogach, *Adv. Opt. Mater.*, 2022, **10**, 2200226.
28 L. Wang, Z. Guan and A. Tang, *J. Nanopart. Res.*, 2020, **22**, 28.
29 K. E. Knowles, K. H. Hartstein, T. B. Kilburn, A. Marchioro, H. D. Nelson, P. J. Whitham and D. R. Gamelin, *Chem. Rev.*, 2016, **116**, 10820–10851.
30 J. Du, R. Singh, I. Fedin, A. S. Fuhr and V. I. Klimov, *Nat. Energy*, 2020, **5**, 409–417.
31 H. Liu, P. Cai, K. J. McHugh, C. F. Perkinson, L. Li, S. Wang, W. Wang, M. Jiao, X. Luo and L. Jing, *Nano Res.*, 2022, **15**, 8351–8359.
32 C. Qiao, Z. Yang, X. Liu, R. Zhang, Y. Xia, L. Wang, Z. Chen, Q. Jia, R. Wang, Y. Yang and Z. Wang, *Nano Lett.*, 2022, **22**, 8250–8257.
33 G. Mahmoud, J. Jedelská, S. M. Omar, B. Strehlow, M. Schneider and U. Bakowsky, *Drug Delivery*, 2018, **25**, 1526–1536.
34 P. Zhang, Y. Feng, L. Zhu, K. Xu, Q. Ouyang, J. Zeng, F. Qin, N. Zhang, Y. Wang, F. He, Y. Shi, G. Chen, Z. Shi, M. Qin, Y. Hou and M. Gao, *Nano Today*, 2023, **48**, 101707.
35 P. Zhang, Y. Qiao, L. Zhu, M. Qin, Q. Li, C. Liu, Y. Xu, X. Zhang, Z. Gan and Y. Hou, *ACS Nano*, 2023, **17**, 184–196.
36 Y. Zhang, Q. Ma, Y. Yan, C. Guo, S. Xu and L. Wang, *Anal. Chem.*, 2020, **92**, 15679–15684.
37 H. Zhong, Y. X. Wu, S. Yu, X. Wang, K. He, D. Li, Y. Cao and N. Gan, *Anal. Chem.*, 2021, **93**, 5691–5699.
38 R. Zhou, S. Sun, C. Li, L. Wu, X. Hou and P. Wu, *ACS Appl. Mater. Interfaces*, 2018, **10**, 34060–34067.
39 J. J. Ma, M. X. Yu, Z. Zhang, W. G. Cai, Z. L. Zhang, H. L. Zhu, Q. Y. Cheng, Z. Q. Tian and D. W. Pang, *Nanoscale*, 2018, **10**, 10699–10704.
40 Y. Y. Yao, G. Gedda, W. M. Girma, C. L. Yen, Y. C. Ling and J. Y. Chang, *ACS Appl. Mater. Interfaces*, 2017, **9**, 13887–13899.
41 Y. Yang, L. Lin, L. Jing, X. Yue and Z. Dai, *ACS Appl. Mater. Interfaces*, 2017, **9**, 23450–23457.
42 S. S. Chetty, S. Praneetha, A. Vadivel Murugan, K. Govarthanan and R. S. Verma, *ACS Appl. Mater. Interfaces*, 2020, **12**, 3415–3429.

43 M. Lv, M. Chen, R. Zhang, W. Zhang, C. Wang, Y. Zhang, X. Wei, Y. Guan, J. Liu, K. Feng, M. Jing, X. Wang, Y.-C. Liu, Q. Mei, W. Han and Z. Jiang, *Cell Res.*, 2020, **30**, 966–979.
44 Y. Jia, H. Liu, P. Cai, X. Liu, L. Wang, L. Ding, G. Xu, W. Wang, M. Jiao and X. Luo, *Chem. Commun.*, 2021, **57**, 4178–4181.
45 M. Jiao, Y. Li, Y. Jia, C. Li, H. Bian, L. Gao, P. Cai and X. Luo, *J. Colloid Interface Sci.*, 2020, **565**, 35–42.
46 M. Jiao, X. Huang, L. Ma, Y. Li, P. Zhang, X. Wei, L. Jing, X. Luo, A. L. Rogach and M. Gao, *Chem. Commun.*, 2019, **55**, 15053–15056.
47 S. Qu, X. Yuan, Y. Li, X. Li, X. Zhou, X. Xue, K. Zhang, J. Xu and C. Yuan, *Nanoscale*, 2021, **3**, 2334–2342.
48 X. Y. Liu, G. Zhang, H. Chen, H. Li, J. Jiang, Y. T. Long and Z. Ning, *Nano Res.*, 2018, **11**, 1379–1388.
49 A. Delices, D. Moodelly, C. Hurot, Y. Hou, W. L. Ling, C. Saint-Pierre, D. Gasparutto, G. Nogues, P. Reiss and K. Kheng, *ACS Appl. Mater. Interfaces*, 2020, **12**, 44026–44038.
50 W. Guo, W. Yang, Y. Wang, X. Sun, Z. Liu, B. Zhang, J. Chang and X. Chen, *Nano Res.*, 2014, **7**, 1581–1591.
51 P. Galiyeva, H. Alem, H. Rinnert, L. Balan, S. Blanchard, G. Medjahdi, B. Uralbekov and R. Schneider, *Inorg. Chem. Front.*, 2019, **6**, 1422–1431.
52 K. Ding, L. Jing, C. Liu, Y. Hou and M. Gao, *Biomaterials*, 2014, **35**, 1608–1617.
53 A. D. P. Leach and J. E. Macdonald, *J. Phys. Chem. Lett.*, 2016, **7**, 572–583.
54 L. Jing, K. Ding, S. Kalytchuk, Y. Wang, R. Qiao, S. V. Kershaw, A. L. Rogach and M. Gao, *J. Phys. Chem. C*, 2013, **117**, 18752–18761.
55 S. Wang, B. R. Jarrett, S. M. Kauzlarich and A. Y. Louie, *J. Am. Chem. Soc.*, 2007, **129**, 3848–3856.
56 L. Jing, K. Ding, S. V. Kershaw, I. M. Kempson, A. L. Rogach and M. Y. Gao, *Adv. Mater.*, 2014, **26**, 6367–6386.
57 H. He, Y. Lin, Z.-Q. Tian, D.-L. Zhu, Z.-L. Zhang and D.-W. Pang, *Small*, 2018, **14**, 1703296.
58 F. Duan, Q. Jia, G. Liang, M. Wang, L. Zhu, K. J. McHugh, L. Jing, M. Du and Z. Zhang, *ACS Nano*, 2023, **17**, 11290–11308.
59 T. Wang, H. Zhang, H. Liu, Q. Yuan, F. Ren, Y. Han, Q. Sun, Z. Li and M. Gao, *Adv. Funct. Mater.*, 2020, **30**, 1906128.